Estimation of Aboveground Carbon Using Different Remote Sensing Data and Modelling Techniques

Hasan AKSOY*1 , Alkan GÜNLÜ2 0

¹Sinop University, Ayancık Vocational School, Ayancık, Sinop, TÜRKİYE ²Çankırı Karatekin University, Faculty of Forestry, Çankırı, TÜRKİYE *Corresponding Author: haksoy@sinop.edu.tr

Received Date: 22.07.2024 Accepted Date: 26.12.2024

Abstract

Aim of study: Forests contribute significantly to the global climate by acting as carbon sinks and controlling energy and water flows. This study aimed to model the aboveground carbon (AGC) of pure Scots pine stands within the boundaries of the Sinop Regional Directorate of Forestry in Turkey, using data obtained from various sensor images, including Sentinel-1 (S1), Sentinel-2 (S2), Landsat 8 OLI (L8) and Unmanned Aerial Vehicle (UAV) images, with artificial neural network (ANN) and multiple linear regression (MLR) modeling techniques.

Area of study: The study was carried out within pure Scots pine stands located in Sinop Regional Directorate of Forestry.

Material and method: a total of 184 sample plots were taken and field measurements were made in these sample plots. 80% of the sample plots (150) were used to fit the models and 20% (34) were used to test the models. The AGC values of each sample plot were estimated with the allometric equation. Brightness values and backscatter values from S1, vegetation indices, reflectance and texture values obtained for different window sizes (3x3, 5x5, 7x7 and 11x11) and different orientations (0°, 45°, 90° and 135°) from L8 and S2, and vegetation indices, band reflectance and digital band obtained from UAV were used in the study.

Main results: The results indicated that the texture variables obtained for the 15x15 of the Sentinel-2 image for AGC estimation, together with the MLR modeling technique, were the most successful technique compared to other images and ANN analysis (R²=0.86).

Research highlights: The results have shown that AGC can be predicted at high success levels with ANN modeling technique with remote sensing data sets.

Keywords: Aboveground Stand Carbon, Natural forests, Modeling, Satellite Images

Farklı Uzaktan Algılama Verileri ve Modelleme Teknikleri Kullanılarak Topraküstü Karbonun Tahmin Edilmesi

Öz

Çalışmanın amacı: Ormanlar, karbonun depolanması, enerji ve su döngülerinin düzenlenmesi gibi süreçlerde küresel iklimde önemli bir rol oynamaktadır. Bu çalışmada Sinop Orman Bölge Müdürlüğü sınırlarında yayılış gösteren saf sarıçam meşcerelerinde Sentinel-1 (S1), Sentinel-2 (S2), Landsat 8 OLI (L8) ve İnsansız Hava Aracı (İHA) gibi farklı uzaktan algılama görüntülerinden elde edilen veriler ile topraküstü karbon (TÜK) arasındaki ilişkiler çoğul doğrusal regresyon (ÇDR) ve yapay sinir ağı (YSA) teknikleri ile modellenmesi amaçlanmıştır.

Çalışma alanı: Çalışma, Sinop Orman Bölge Müdürlüğü'nde bulunan saf sarıçam meşcerelerinde gerçekleştirilmiştir.

Materyal ve yöntem: Çalışma kapsamında toplam 184 adet örnek alan alınmış ve bu örnek alanlarda yersel ölçümler yapılmıştır. Alınan örnek alanların %80'i (150 adet) modellerin oluşturulmasında, %20'si (34 adet) ise modellerin test edilmesinde kullanılmıştır. Her bir örnek alanın TÜK değerleri allometrik denklem ile tahmin edilmiştir. Çalışmada uzaktan algılama verisi olarak, S1 görüntüsünden geri saçılma ve bant parlaklık değerleri, S2 ve L8 uydu görüntüleri için farklı pencere boyutlarına (3x3, 5x5, 7x7 ve 11x11) ve farklı yönelimlere (0°, 45°, 90° ve 135°) göre yansıma değerleri, vejetasyon indeksleri ve doku özellikleri ile İHA görüntülerinden elde edilen dijital bant, bant reflektans ve vejetasyon indisleri kullanılmıştır. Yersel ölçümler ve uzaktan algılama verileri arasındaki ilişkiler ÇDR ve YSA teknikleri ile modellenmiştir.

Temel sonuçlar: Sonuçlar, TÜK tahmininde S2 görüntüsünün 15x15 pencere boyutu için elde edilen doku değişkenleri ÇDR modelleme tekniği ile birlikte diğer görüntülere ve YSA analizine kıyasla en başarılı teknik olduğunu göstermiştir (R²=0.86).

Āraştırma vurguları: Sonuçlar, TÜK'ün uzaktan algılama veri setleri ile ÇDR modelleme tekniği ile yüksek başarı düzeylerinde tahmin edilebileceğini göstermiştir.

Anahtar Kelimeler: Topraküstü Meşcere Karbonu, Doğal orman, Modelleme, Uydu Görüntüleri



Introduction

As a major component of terrestrial ecosystems, forests play a crucial role in maintaining ecological balance (Wu et al., 2020; Zhang et al., 2022). In addition, forests are the largest carbon sink in these ecosystems (Zaninovich & Gatti, 2020). Forests contribute to carbon sequestration by absorbing 76% to 98% of the carbon present in terrestrial ecosystems (Cheng et al., 2009) and playing a key role in combating global warming caused by carbon emissions (Wang et al., 2013). According to report of the IPCC, the Earth's temperature increased by 1.2 °C between 1850 and 1900 (Mu et al., 2022; Aksoy, 2024). In recent years, when population and industrialization increased rapidly, forests have emerged as the most effective and cost-efficient means of combating global warming. Since forests are the primary carbon sink on land, shifts in their carbon storage lead to changes in atmospheric carbon dioxide, thereby directly influencing global climate change (Fu, 2018; Liu et al., 2020; Zhang et al., 2022; Seki & Atar, 2021). All this information shows that forests offer great potential for sequestering atmospheric carbon. Therefore, in recent years there has been an urgent need to measure forest carbon stocks accurately, quickly, efficiently, and reliably (Romanov et al., 2022; Zhang et al., 2023). The most common method of determining above-ground carbon (AGC) is either by cutting the tree and calculating the amount of its biomass and carbon based on the biomass value or by carbon analysis of wood materials (Bi et al., 2015). However, this destructive method requires a lot of labor, time, and cost. In addition, the fact that local measurements require a lot of fieldwork, each fieldwork damages the forest ecosystem, and it is not practical to use it in large forest areas (Xu et al., 2022; Zhang et al., 2023; Aksoy and Günlü, 2025).

Developments in sensing remote technology forest enable monitoring resources and are used as an alternative source information traditional field to measurements. In particular, the real-time, fast, and broad-scale monitoring of areas has made it a popular source of information widely used in forestry, environment, and ecology (Fremout et al., 2022). Recently, there has been a rise in initiatives to combine remote sensing data with ground-based inventory data to achieve reliable and costeffective AGC estimation over extensive areas. Optical data, LiDAR, SAR data, and integrated remote sensing data derived from the combination of these sources are utilized for AGC estimation (Georgopoulos et al., 2022). A wide range of spectral and textural data is provided by optical sensors (band information, vegetation indices, texture characteristics, etc.) and are often used to estimate stand parameters (Chrysafis et al., 2019). Landsat and Sentinel-2 which are easy and inexpensive to access from optical sensors, are the most widely used data sources in research. The first satellite for natural resources, Landsat imagery, has traditionally been employed to assess stand parameters across large forested areas (Zheng et al., 2004; Günlü et al., 2014; Yavaşlı & Ölgen, 2017; Sakici & Günlü 2018; Turgut & Günlü, 2022; Bulut, 2023). The upgraded multispectral imager of Sentinel-2, with improved spatial resolution, includes three red-edge bands that are essential for accurately estimating the distribution and parameters of forest resources. Sentinel-1 C (SAR) active satellite imagery has all-weather imaging capability and is widely used for estimating stand parameters (Udali et al., 2021). Moreover, Radar and airborne LIDAR (ALS) data are frequently utilized for AGC estimation because of their ability to penetrate dense vegetation (Lu et al., 2012; Silva et al., 2018; Zhang et al., 2023). ALS data is costly to obtain and not spatially continuous, limiting AGC estimation in large forested areas (Listopad et al., 2011; Ehlers et al., 2022). Recently, rapidly developing unmanned aerial vehicles (UAVs) have also been used to estimate stand parameters and monitor forests. The advantages of UAVs, such as low cost, fast and less risky high-resolution and simple data collection, complement the shortcomings of traditional remote sensing (Lan et al., 2019; Aksoy, 2022; Aksoy, 2024). Some studies have found that AGC can be accurately estimated using high-resolution UAV imagery and tree height and crown data (Jucker et al., 2017; Fermandes et al., 2020).

Both parametric and non-parametric models are utilized in remote sensing-based

AGC estimation (Huang et al., 2019). The parametric model is highly regarded for its ability to assess the relationship between AGC and independent variables (Ou et al., 2019). Multiple linear regression (MLR), a widely used method, is particularly valued for its simplicity, ability to identify variables, and strong performance in AGC estimation (Li et al., 2020a). In addition, artificial neural networks (ANN) (Dong et al., 2019; Günlü et al., 2021; Zhang et al., 2023), k-nearest neighbor (k-NN) (Zhang et al., 2022), random forest (RF) (Li et al, 2020; Tang et al., 2022), support vector machine (SVM) (Sivasankar et al., 2013; Han et al., 2021), maximum entropy (MaxEnt) (Wang et al., 2022), extreme gradient boosting (XGBoost) (Li et al., 2020b), multivariate adaptive regression splines (MARS) (Baloloy et al. 2018) were used modeling AGC. ANN, a non-parametric modeling technique, is widely used in AGC modeling (Alquraish & Khadr, 2021; Wang et al., 2022; Zhang et al., 2023). Additionally, ANN, which is part of artificial intelligence and imitates the function of the human brain, has become increasingly utilized in forestry applications (Strobl & Forte, 2007; Ogana & Ercanlı, 2022). Artificial neural networks have been frequently used by researchers in forestry, with significant success in predicting tree height, tree volume, tree biomass and carbon (Hamidi et al., 2021; Ogana & Ercanlı, 2022). The study data are less affected by the above-mentioned disadvantages of ANN models against the low success levels that may occur with MLR modeling due to a nonconstant variance distribution in MLR modeling and the possibility of linearity of explanatory variables, and accordingly higher success levels can be achieved (Guisan et al., 2002; Aertsen et al., 2010). Therefore, ANN modeling technique was also used in this study.

In this study, (i) the relationships between AGC values calculated using data obtained from ground measurements with data obtained from Sentinel-1, Sentinel-2, Landsat 8 OLI and UAV images were modeled using ANN and MLR modeling techniques, (ii) the results of the two modeling techniques were compared to investigate which modeling technique is more successful in AGC estimation.

Material and Methods

Study Area

The study was conducted within the boundaries of the Sinop Regional Directorate of Forestry (RDF), which is located in the northernmost part of Turkey. It is located between 600000 and 710000 E longitude and, 4560000 and 4665000 N latitude. The total area of Sinop RDF is 556275.50 ha and the total area of pure Scots pine stands is 7548.49 ha. Since the study area receives rainfall at all times of the year, it is covered with rich and diverse forest cover. The average annual rainfall is 685.7 mm in the study area, which receives the most precipitation in October and the least in May. Pinus sylvestris, Abies nordmanniana, Fagus orientalis, Pinus nigra, Carpinus betulus, Quercus spp., Fraxinus excelsior, Juniperus sp., Populus tremula and *Ulmus* sp. are the most common tree species in Sinop RDF. The average annual temperature of the study area is 14 °C (GDF, 2022). The map in Figure 1 provides the geographical location of the study area.

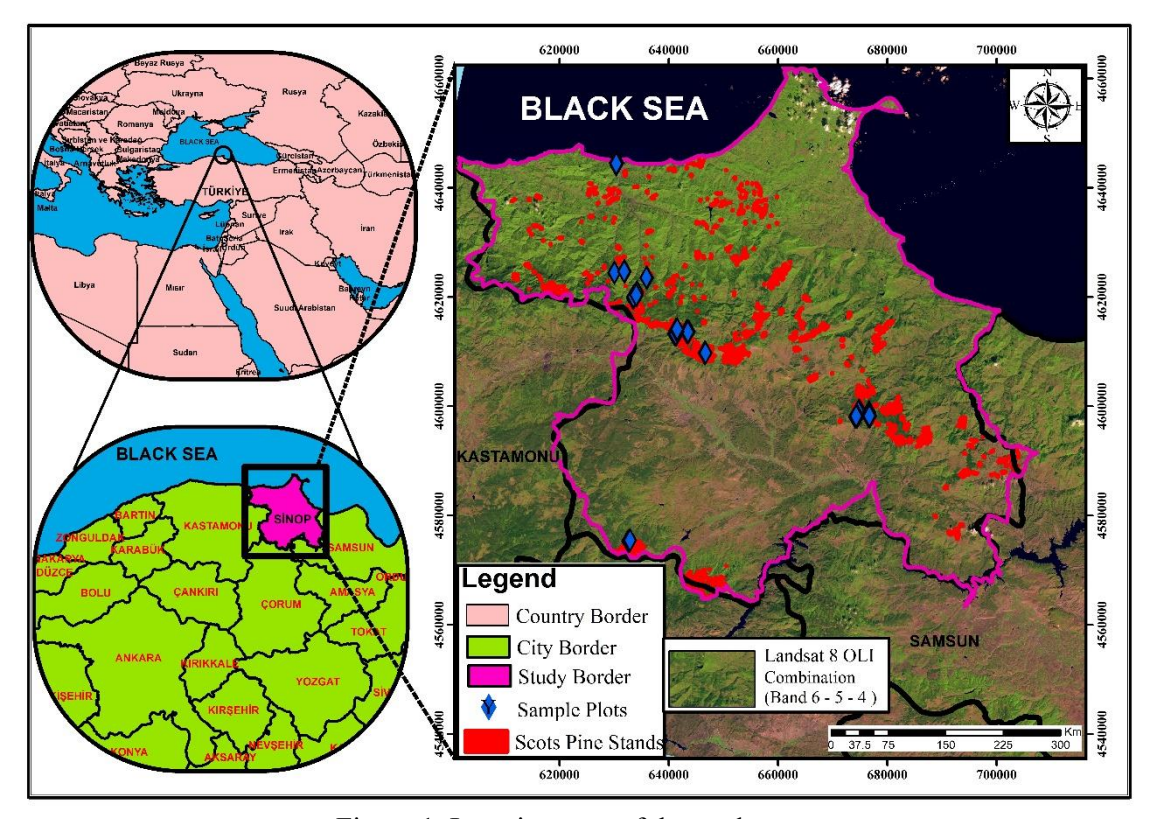


Figure 1. Location map of the study area

Field Measurements

A total of 184 sample plots with different site index, crown closure and development stages classes were used for above-ground carbon (AGC) field measurements in this Traditional study. forest inventory measurements were made in the sample plots determined for the estimation of AGC values. Sample plots were assigned sizes of 800 m² (11-40%), 600 m² (41-70%), and 400 m² (71-100%), according to the crown closure. In each sample plot, the diameter at breast height of trees with a diameter of 8 cm or greater was measured. To estimate the AGC of the trees in the sample plots, the allometric equation (Eq. 1) developed by Yavuz et al. (2010) for pure Scots pine stands was used. The total AGC for each plot was computed by adding up the AGCs of all the trees in the respective sample plot.

$$AGC = -28.360 + 0.413 \times d_{1.3} \tag{1}$$

Where:

AGC: Aboveground carbon, $d_{1,3}$: Tree diameter at breast height.

Satellite Data and Image Processing

Landsat 8 OLI (L8), Sentinel-2 (S2), Sentinel-1 (S1) and Unmanned Aerial Vehicle (UAV) images were used. The S1 (October 17, 2021) with a dual-polarized VV/VH image downloaded was from https://scihub.copernicus.eu. The S2 (October 15, 2021) with 13 spectral bands and L8 (September 26, 2021) with 11 spectral bands were downloaded from https://earthexplorer.usgs.gov. Finally, UAV images of the study area were taken by DJI Inspire-2 drone between August and October 2021. S2 at 20 m and 10 m, L8 at 30 m and 15 m, and UAV imagery at resolutions between 2.5 cm and 3.5 cm were used in the study. Figure 2 presents the details of the UAV and camera specifications used in the study.



DJI Inspire 2		DЛ Zenmuse X-5S
Maximum take-off weight	8.82lbs (4000g)	Micro Four Thirds sensor
Maximum flight time	Approx. 27 min (with zenzenx4s)	5.2K video recording at 30fps and 4K at 60fps
Operating temperature	-4° to 104°F (-20° to 40°C)	20.8 MP still image capture
Battery capacity	4280mAh	12.8 stops of dynamic range
Maximum speed	58 mph or 94 kph (sport mode)	12-bit raw photos
Energy	97.58Wh	20fps continuous burst shooting
Voltage	22.8V	
Туре	quadcopter	
Live view	1080p	

Figure 2. Technical specifications of the UAV platform and optical sensor

In the study, pre-processing of S1 from remote sensing data sets was performed in SNAP. Band brightness and backscattering (dB) values of VH and VV polarizations were calculated from the S1. First, the image was preprocessed in SNAP using the "Graph Builder" tool in a total of 8 steps, including (i) read to image (ii) apply-orbit file (iii) thermal noise removal (iv) calibration (v) speckle filter (vi) terrain correction (vii) dB to linear (viii) write to image and made ready for analysis. The obtained images were overlaid with sample plot polygons in ArcGIS 10.7. With the overlay, one-to-one inference was made according to the sample plot boundary and data was obtained from all pixels corresponding to the boundary. Finally, using the "zonal statistics" tool in ArcGIS 10.7, dB values and numerical band values of VH and VV polarizations were acquired for each sample plot and S1 data sets were prepared for modeling. QGIS 3.8.1 version was used for the pre-processing of S2 and L8. The images

were calibrated using the Semi-Automatic Classification "Plugin" tool, which includes the calibration of satellite images, and reflectance images were obtained for each band. The obtained images were overlaid with sample plot polygons in ArcGIS 10.7TM as in the creation of the S1 dataset and reflectance values were calculated for each sample plot using the "zonal statistics" tool. A total of 12 vegetation indices were computed for S2 and L8 using reflectance values (Table 1). In addition, data sets with different texture characteristics were created from S2 and L8 using ENVI 5.2. These datasets include variance (VAR), mean (M), correlation (COR), homogeneity (HOM), entropy (ENT), dissimilarity (DIS), second moment (SM) and contrast (CONT) from satellite imagery, and separate datasets for different window sizes (3x3, 5x5, 7x7, 9x9, 11x11, 13x13, and 15x15) and different orientations (0° , 45°, 90°, 135°).

Table 1. Formulas for vegetation indices obtained from Sentinel-2, Landsat 8 and UAV images

Vegetation indices	Sentinel 2 Formulas	Landsat 8 OLI Formulas	Reference
NDVI (Normalized Difference Vegetation Index)	(B8 - B4) / (B8 + B4)	(B5-B4) / (B5+B4)	Rouse et al. (1974)
MSI (Moisture Stress Index)	(B11 / B8)	(B6/B5)	Hunt and Rock (1989)
NBR (Normalized Burn Ratio)	(B8 - B12) / (B8 + B12)	(B5-B7) / (B5+B7)	Key and Benson (2006)
EVI (Enhanced Vegetation Index)	2.5 x (B8 - B4) / ((B8 + 6.0 x B4 - 7.5 x B2) + 1.0)	$2.5 \times ((B5 - B4) / (B5 + 6 \times B4 - 7.5 \times B2 + 1))$	Liu and Huete (1995)
SAVI (Soil Adjusted Vegetation Index)	(B8 - B4) / (B8 + B4 + L) x (1.0 + L); L = 0.428	((B5-B4)/(B5+B4+0.5)) $\times (1.5)$	Huete (1988)
DVI (Difference Vegetation Index)	(B8 / B4)	(B5 - B4)	Tucker (1980)
GNDVI (Green Normalized Difference Vegetation Index)	(B8 - B3) / (B8 + B3)	(B5 - B3) / (B5 + B3)	Gitelson et al. (1996)
NDWI (Normalized Difference Water Index)	(B8-B11) / (B8+B11)	(B5 - B6) / (B5 + B6)	McFeeters (1996)
MSR (Modified Simple Ratio)	(B8 - B1) / (B4 - B1)	((B5 / B4) -1) / √ ((B5 / B4) +1)	Chen (1996)
NLI (Nonlinear vegetation index)	(B8 - B4) / (B8) + B4)	((B5) - B4) / ((B5) + B4)	Goel and Qin (1994)
PSSR (Pigment Specific Simple Ratio)	(B8 / B4)	(B5 / B4)	Blackburn (1998)
EVI2 (Enhanced Vegetation Index 2)	2.4 x (B8 - B4) / (B8 + B4 + 1.0)	2.4 x (B5 - B4) / (B5 + B4 + 1.0)	Jiang et al. (2008)
UAV Vegetation indices	UAV Formulas	Reference	
RGBVI (Red-Green-Blue Vegetation Index)	$(G \times G)$ - $(R \times B)/(G \times G)$ + $(R \times B)$	Bendig et al. (2015)	
GLI (Green Leaf Index)	$(2 \times G - R - B) / (2 \times G + R + B)$	Louhaichi et al. (2001)	
VARI (Visible Atmospherically Resistant Index)	$\left(\text{G-R} \right) / \left(\text{G} + \text{R-B} \right)$	Gitelson et al. (2002)	
NGRDI (Normalized Green Red Difference Index)	$\left(G\text{-R}\right) /\left(G\text{+R}\right)$	Tucker (1979)	
ERGBVE (Enhanced Red-Green-Blue Vegetation Index)	$\pi \ x \ ((G^2\text{-}(R \ x \ B)) \ / \ (G^2 + (R \ x \ B))$	Themistocleou (2019)	
GR (Simple red-green ratio)	R/G	Gamon and Surfus. (1999)	
RGBVI2 (RGB-based vegetation index 2)	(G-R)/B	García-Fernández et al. (2021)
TGI (Triangular Greenness Index)	G-0.39 x R-0.61 x B	Hunt et al. (2013)	
GRVI (Green-red vegetation index)	(G-R)/(G+R)	Tucker (1979)	
MGRVI (Modified green–red vegetation index)	$(G^2-R^2)/(G^2+R^2)$	Bendig et al. (2015)	
BG12 (Simple blue-green ratio)	B/G	Zarco-Tejada et al. (2005)	
VEG (Vegetativen)	G / (Ra x B(1-a)); a=0.667	Hague et al. (2006)	
EXG (Excess green index)	2G – R- B	Woebbecke et al. (1995)	
NGBDI (Normalized green-blue difference index)	$\left(G-B\right)/\left(G+B\right)$	Du and Noguchi (2017)	
RGBVI3 (RGB-based vegetation index 3)	(G+B)/R	García-Fernández et al. (2021)

UAV Data and Image Processing

UAV images for the study were captured for each sample plot using a DJI Inspire-2 drone. Flight plans were then developed to cover each sample plot, taking into account the drone's battery capacity (Figure 3). Sixteen flight plans were created to cover all the sample plots within the study area. For each flight plan, the UAV's takeoff point and corresponding altitude were identified. The

minimum flight altitude was then calculated based on these two altitude values. As a result, the flight altitude was standardized at 120 meters to maintain consistency across all flight parcels. Additionally, to achieve the study's objectives, the image overlap ratios for the front and sides were set at 80% and 70%, respectively. The camera angle was fixed at 90° (nadir) for all flights, and the flights were conducted accordingly.

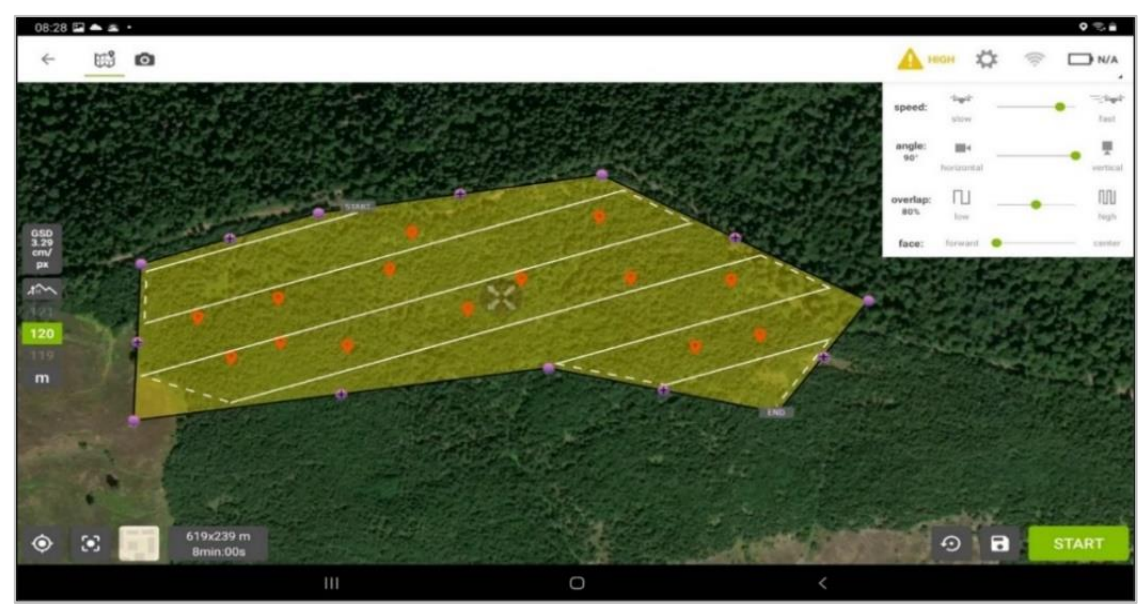


Figure 3. UAV flight line and photo location, red points represent the sample plot centers where field measurements were conducted, the black polygon represents the boundary of the flight, and the white lines represent the path followed by the UAVs during the image capture phase

After the images were taken, orthomosaic, digital terrain model (DTM), digital surface model (DSM) and reflectance (red, green, blue, and grayscale) images of the sample plots were created. The images of all parcels included in the study consist of three bands: red, green, and blue. Additionally, a grayscale (panchromatic) band was generated as a fourth band, as described in Equation 2, resulting in images composed of a total of four bands.

The production of orthomosaic, DTM, and DSM maps from UAV images was carried out in 3 main stages in PIx4D. In the first stage, the images were aligned and all images were calibrated for the relevant flight parcel using camera internal and external orientation parameters and tie points were created. In the second stage of the production process, a point

cloud and solid model were created from the calibrated images. Then, the point cloud data were classified and DTM was generated. In addition, the images were grouped together with the 3D texture solid model. In the last and third stage, first the DSM filter was applied and then the DSM raster image was created. Then orthomosaic and DTM raster images were created. Finally, reflectance images (red, green, blue, and grayscale) and the index image of the study area obtained by combining these bands were created (Figure 4). In creating orthophotos and reflectance images of the flights, 15 vegetation indices were computed from the satellite images using ArcGIS 10.7TM, and 15 vegetation indices were calculated from the UAV images (Table 1).

$$Greyscale = 0.0722 \times Blue + 0.7152 \times Green + 0.2126 \times Red$$
(2)

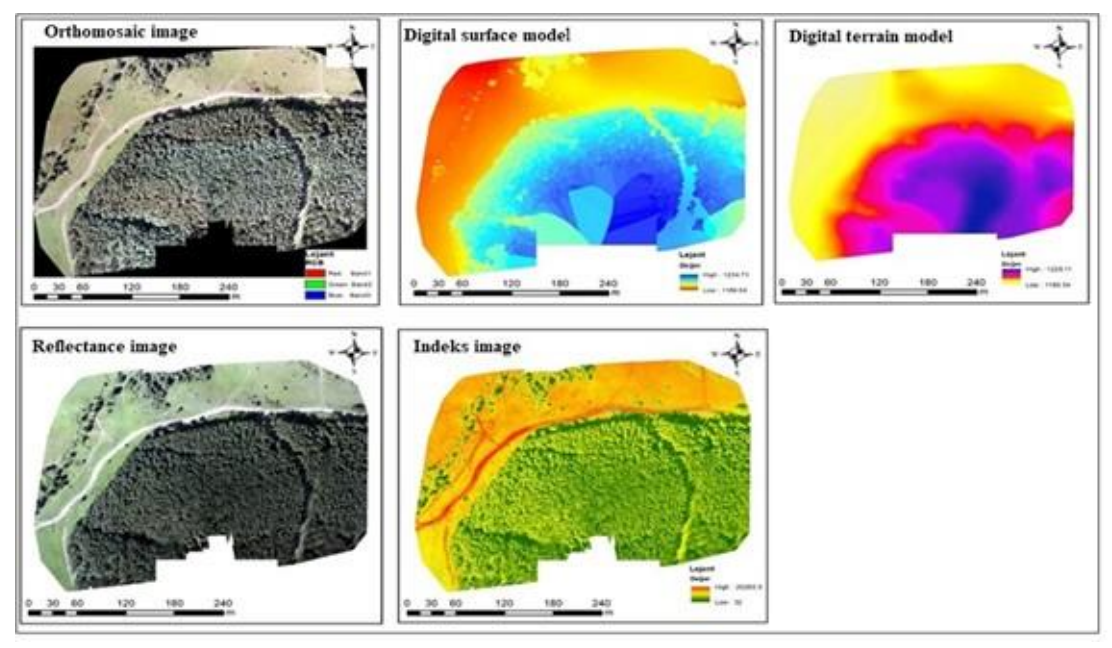


Figure 4. Data obtained from UAV images (Sakız forest planning unit, Flight parcel no. 1)

Modelling

In the modeling stage, data sets were prepared to model the relationships between reflectance, vegetation indices, texture features, backscatter, and digital band values derived from S1, S2, L8, and UAV images, and AGC obtained from field measurements. Total 184 sample plots used in the study, 80% (150 sample plots) were utilized for model training, while 20% (34 sample plots) were reserved for model testing. MLR and ANN methods were employed for modeling the datasets, and the process took place in three phases.

In the first stage, AGC was estimated through MLR using remote sensing data. In the second stage, the prediction models, developed from the training data sets, were applied to generate predictions for the test data. In the third stage, a paired t-test was performed to evaluate whether a significant difference existed between the predicted results and the observed data.

Multiple linear regression analysis

MLR was employed to model the relationship between AGC and remote sensing data, with the model structure outlined in Equation 3.

$$AGC = \beta_0 + \beta_1 \cdot X_1 + \beta_2 \cdot X_2 + \dots + \beta_n \cdot X_n + \varepsilon$$
 (3)

The AGC was selected as the dependent variable in the model, while the independent variables $(X_1, X_2, ..., X_n)$ consisted of remote sensing data derived from S1, S2, L8, and UAV imagery. These data included texture features, vegetation indices, reflectance, digital band, brightness and backscattering values. The coefficients β_0 , β_1 , β_2 , ..., β_n represent the model parameters, and ϵ denotes the additive bias.

Bayesian artificial neural networks

Another modeling approach employed in the study to estimate AGC is ANN. In this technique, the independent variables were derived from remote sensing data such as brightness, backscatter, vegetation indices, reflectance, texture features and digital band values that were found to be significant for AGC estimation in the MLR method. MATLAB codes with various ANN model configurations were utilized in the study (Bolat, 2021). Although the network designed in ANN models yields good results for training datasets, it may perform poorly on the test dataset, or vice versa. This phenomenon is known as overfitting or misfit, and it represents one of the major drawbacks of ANN. Overfitting is particularly inevitable for

ANN models with small training datasets. Various approaches have been proposed to address the overfitting issue in ANN models. One such approach involves selecting an appropriate regularization training function, such as Levenberg-Marquardt or Bayesian methods (Van Havre et al., 2015; Okut, 2016; Bolat, 2021; Skudnik & Jevsenak, 2022; Seki, 2023). Since Bayesian network structures have early stopping capability and are more compatible with the regularization parameter, Bayesian network structure is used in ANN modeling in this study. In ANN models, independent variables can be normalized using various techniques to enhance network complexity and improve robustness against outliers (Akıllı & Hülya, 2020). In this study, the independent variables were normalized using the min-max technique, transforming the data into values ranging from -1 to +1 (Foresee & Hagan, 1997). Normalizing the variable data within this range enhances the generalization capability of the Bayesian network structure. The hyperbolic tangent transfer function was used in this study, as the data were organized within the [-1, 1] range. influencing Another factor network performance is the learning rate and momentum values. The momentum value is typically chosen between 0 and 1. The learning rate is a critical parameter in the network's training process; a small learning rate can lead to overfitting, while a large learning rate may result in underfitting and large errors (Lawrence et al., 1997). Therefore, selecting appropriate learning rate and momentum values simultaneously is crucial for optimizing network performance (Bolat, 2021). In this study, based on the learning rate and momentum values, 17 models were developed for AGC. These included 9 models where the learning rate was fixed at 0.1 and momentum varied between 0.1 and 0.9, and 8 models where momentum was fixed at 0.1 and the learning rate varied

between 0.1 and 0.9. Finally, model performance criteria were evaluated and the most successful model among the 17 models was selected. Each model obtained is numbered from 1 to 17 as AGC1,, AGC17. Here AGC1 refers to the first model obtained in the ANN modeling technique.

Model performance criteria

The predictive power of the models was assessed using several evaluation metrics, including the coefficient of determination $(R^2_{adj}, Eq. 4)$, root mean squared error (RMSE, Eq. 5), mean absolute error (MAE, Eq. 6), bias (Bias, Eq. 7), Akaike's information criterion (AIC, Eq. 8), and Bayesian information criterion (BIC, Eq. 9), all of which were calculated as described in Table 2. It is important to note that a model that performs well according to one criterion may not necessarily perform well according to another. To address this, the Relative Ranking Method proposed by Poudel and Cao (2013) was employed, which takes all criteria into account when selecting the most successful model (Rj, Eq. 10). In this approach, all success criteria are considered and ranked relatively based on their proximity and distance values. The Ri values calculated for each performance criterion are then summed, and the model with the smallest total Ri value is considered the most successful for the relevant criterion (Sakici & Ozdemir, 2018; Ercanlı et al., 2018). Explanations of the formulas are provided in Table 2, where n represents the number of observations, p is the number of parameters, yi are the measured AGC values, \hat{y}_1 are the predicted AGC values, and \overline{y}_i is the mean of the measured AGC values. R_i is the relative rank of method i (i = 1, 2, 3, ..., m), k denotes the number of coefficients, Si refers to the goodness of fit statistics generated from the methods, Smin is the minimum value of Si, and Smax is the maximum value of Si.

Table 2. Formulas for model performes criteria	
$R^{2} = 1 - \frac{\sum_{i=1}^{n} (y_{g} - y_{t})^{2}}{\sum_{i=1}^{n} (y_{g} - y_{og})^{2}}$	(4)
$\sum_{i=1}^{n} (y_g - y_{og})^2$	
$RMSE = \sqrt{\frac{1}{n} \sum_{i=1}^{n} (y_i - \widehat{y}_i)^2}$	(5)
$MAE = \frac{1}{n} \sum_{i=1}^{n} y_i - \widehat{y_i} $	(6)
$Bias = \frac{\sum_{i=1}^{n} (y_i - \hat{y_i})}{n}$	(7)

$$Bias = \frac{\sum_{i=1}^{n} (y_i - \widehat{y}_i)}{n} \tag{7}$$

$$AIC = \ln(RMSE) + 2k \tag{8}$$

$$BIC = \ln(RMSE) + \ln(k) \tag{9}$$

$$R_{j} = 1 + \frac{(m-1)(S_{i} - S_{min})}{S_{max} - S_{min}}$$
(10)

The study's methodology can be generally outlined in three key stages. The first step involves calculating the AGC using data obtained from field measurements. In the second step, images from S1, S2, L8, and UAV are processed to generate data sets. In

the third and final step, AGC is estimated using MLR and ANN modeling techniques with the generated data sets, followed by the evaluation of model performance. The overall workflow of the methodology is illustrated in Figure 5.

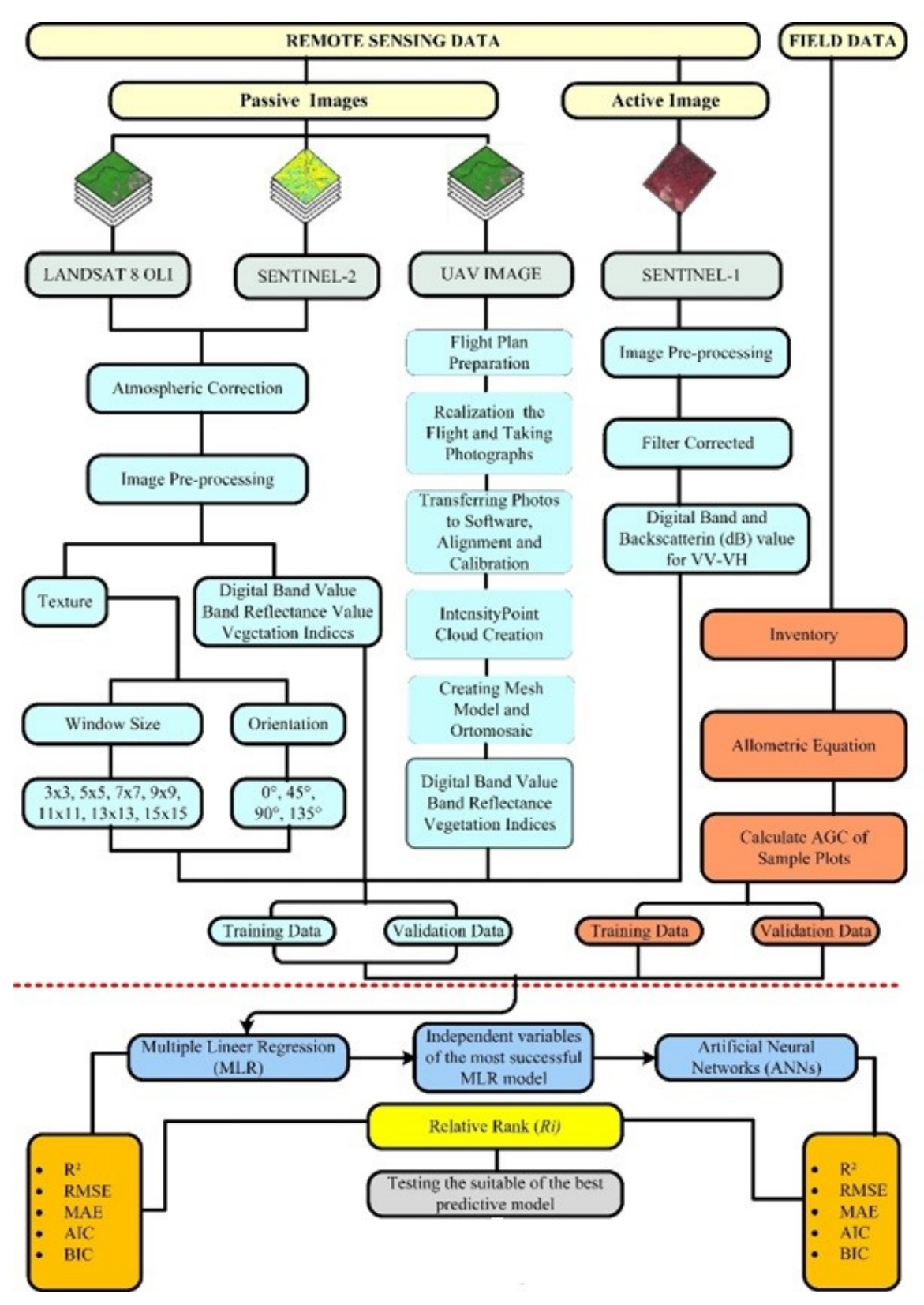


Figure 5. Flowchart of the methodology of the study

Result

Multiple Linear Regression Analysis

Table 3 presents the success criteria values and total relative ranks for the relationships between AGC and remote sensing data, utilizing the MLR technique. A review of Table 3 reveals that the models corresponding to the dataset with the lowest total relative ranks are identified as the most successful. The highest success with reflectance data was recorded for the L8 ($R^2_{adj} = 0.41$), while the lowest success was observed for the UAV ($R^2_{adj} = 0.24$). For vegetation indices, the S2 showed the highest success ($R^2_{adj} = 0.64$), whereas the UAV data yielded the lowest success ($R^2_{adj} = 0.34$). When analyzing the

model results for texture features from L8 and S2, the highest success was achieved with the 15x15 window size of the S2 ($R^2_{adj} = 0.86$), while the lowest success was recorded with the 3x3 window size of the L8 ($R^2_{adj} = 0.71$). In terms of texture feature orientation, the L8 dataset showed the highest success at 0° (R²_{adi} = 0.86), while the S2 had the lowest success at 135° (R²_{adj} = 0.59). This study did not develop any analytical model using UAV digital band datasets. Models derived from the backscatter and digital band data of the S1 demonstrated relatively low success. Figure 6 depicts the variation of the models based on the coefficient of determination and total relative rank.

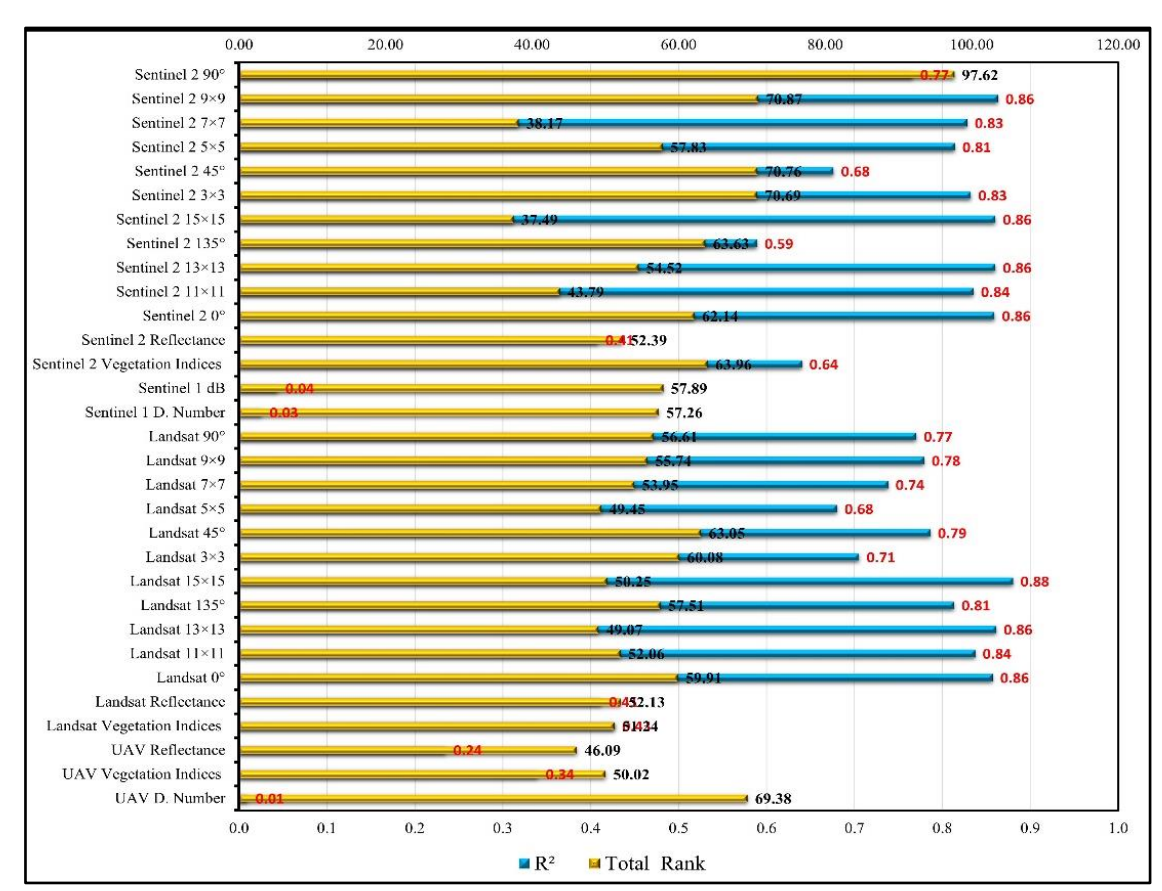


Figure 6. The variation of models obtained from remote sensing data according to the coefficient of determination and total relative rank numbers

When analyzing the success criteria of the MLR model applied to AGC, the highest success in remote sensing datasets was achieved with texture datasets (Table 3). Specifically, the variation in the dataset through different window sizes and

orientation sizes greatly enhanced the model outcomes. The highest coefficient of determination for AGC using different filters was obtained in the 15x15 window size for texture features obtained from the S2 (Table 4).

Table 3. Values for the success criteria and total relative ranks in the MLR

Dataset	Training						Training Relative Rank					
Dataset	\mathbb{R}^2	RMSE	MAE	BIC	AIC	\mathbb{R}^2	RMSE	MAE	BIC	AIC	Total	
UAV DN	-	-	-	-	-	-	-	-	-	-	-	
UAV VIs	0.34	88.43	74.79	5.18	8.48	19.62	17.50	1.04	9.12	2.74	50.02	
UAV RV	0.24	95.56	76.72	4.56	6.56	23.24	19.81	1.04	1.00	1.00	46.09	
L8 VIs	0.43	82.45	66.70	5.51	10.41	16.62	15.55	1.03	13.54	4.49	51.24	
L8 RV	0.41	83.19	65.86	5.52	10.42	17.14	15.80	1.03	13.66	4.50	52.13	
L8 Orientation (0°)	0.86	38.89	30.85	6.49	37.66	1.79	1.41	1.00	26.51	29.20	59.91	
L8 Window Size (11×11)	0.84	42.24	31.77	6.31	29.74	2.48	2.49	1.00	24.06	22.02	52.06	
L8 Window Size (13×13)	0.86	39.03	30.71	6.23	29.66	1.66	1.45	1.00	23.02	21.95	49.07	
L8 Orientation (135°)	0.81	45.07	34.99	6.45	31.81	3.31	3.41	1.00	25.89	23.89	57.51	
L8 Window Size (15×15)	0.88	37.64	29.33	6.27	31.63	1.00	1.00	1.00	23.52	23.73	50.25	
L8 Window Size (3×3)	0.71	57.47	45.03	6.45	26.05	7.03	7.44	1.01	25.92	18.67	60.08	
L8 Orientation (45°)	0.79	48.06	38.31	6.58	33.87	4.24	4.38	1.01	27.65	25.76	63.05	
L8 Window Size (5×5)	0.68	60.53	36.15	6.05	18.10	7.90	8.44	1.01	20.64	11.47	49.45	
L8 Window Size (7×7)	0.74	54.15	43.43	6.29	23.99	5.90	6.36	1.01	23.88	16.80	53.95	
L8 Window Size (9×9)	0.78	49.43	38.14	6.39	27.90	4.48	4.83	1.01	25.08	20.35	55.74	
L8 Orientation (90°)	0.77	50.35	38.08	6.40	27.92	4.79	5.13	1.01	25.32	20.36	56.61	
S1 DN	0.03	104.03	86.55	4.64	6.64	30.45	22.57	1.04	2.12	1.08	57.26	
S1 dB	0.04	106.78	87.48	4.67	6.67	29.83	23.46	1.04	2.46	1.10	57.89	
S2 VIs	0.64	78.59	50.55	6.44	20.36	9.28	14.30	1.02	25.85	13.52	63.96	
S2 RV	0.41	83.45	67.98	5.52	10.42	17.28	15.88	1.03	13.70	4.50	52.39	
S2 Orientation (0°)	0.86	38.51	31.02	6.54	39.65	1.72	1.28	1.00	27.13	31.00	62.14	
S2 Window Size (11×11)	0.84	43.10	32.66	6.07	23.76	2.55	2.77	1.00	20.87	16.60	43.79	
S2 Window Size (13×13)	0.86	38.88	30.51	6.37	33.66	1.69	1.40	1.00	24.86	25.57	54.52	
S2 Orientation (135°)	0.59	68.04	51.93	6.42	22.22	11.03	10.88	1.02	25.50	15.20	63.63	
S2 Window Size (15×15)	0.86	39.74	31.17	5.88	21.68	1.69	1.68	1.00	18.41	14.71	37.49	
S2 Window Size (3×3)	0.83	54.66	32.73	6.83	38.00	2.66	6.53	1.00	31.00	29.50	70.69	
S2 Orientation (45°)	0.68	59.35	45.29	6.72	32.08	8.03	8.05	1.01	29.52	24.14	70.76	
S2 Window Size (5×5)	0.81	45.63	29.40	6.46	31.82	3.28	3.59	1.00	26.06	23.90	57.83	
S2 Window Size (7×7)	0.83	44.19	33.57	5.87	19.79	2.79	3.13	1.00	18.25	12.99	38.17	
S2 Window Size (9×9)	0.86	38.79	28.58	6.22	29.66	1.59	1.37	1.00	22.94	21.94	70.87	
S2 Orientation (90°)	0.77	50.07	38.91	6.69	35.91	4.93	5.04	1.04	29.04	27.61	97.62	

Table 4. Above ground carbon model generated using the 15x15 window size texture data from the S2

Independent variables	Coefficients of Independent variables	t statistics	p-value
Constant	-3500.740	-8.807	0.000
COR_S2_15_90°	192.946	6.298	0.000
SM_S5_15_135°	-2010.659	-4.265	0.000
CON_S6_15_0°	-91.207	-3.802	0.000
COR_S5_15_90°	-300.979	-6.092	0.000
SM_S7_15_0°	-512.740	-9.566	0.000
OM_S4_15_135°	3599.181	9.218	0.000
M_S7_15_135°	98.795	4.633	0.000
DIS_S4_15_135°	1148.961	7.969	0.000
CON_S6_15_45°	52.021	10.808	0.000
VAR_S2_15_0°	-131.609	-1.932	0.055
SM_S5_15_0°	3034.135	6.547	0.000
DIS_S4_15_0°	632.743	4.802	0.000
SM_S3_15_90°	236.889	8.673	0.000
CON_S7_15_0°	-197.697	-3.841	0.000

S: Sentinel-2, S12: Band 12 of Sentinel-2, HOM: homogeneity, CONT: contrast, COR: correlation, DIS: dissimilarity, M: mean, VAR: variance, ENT: entropy and SM: second moment

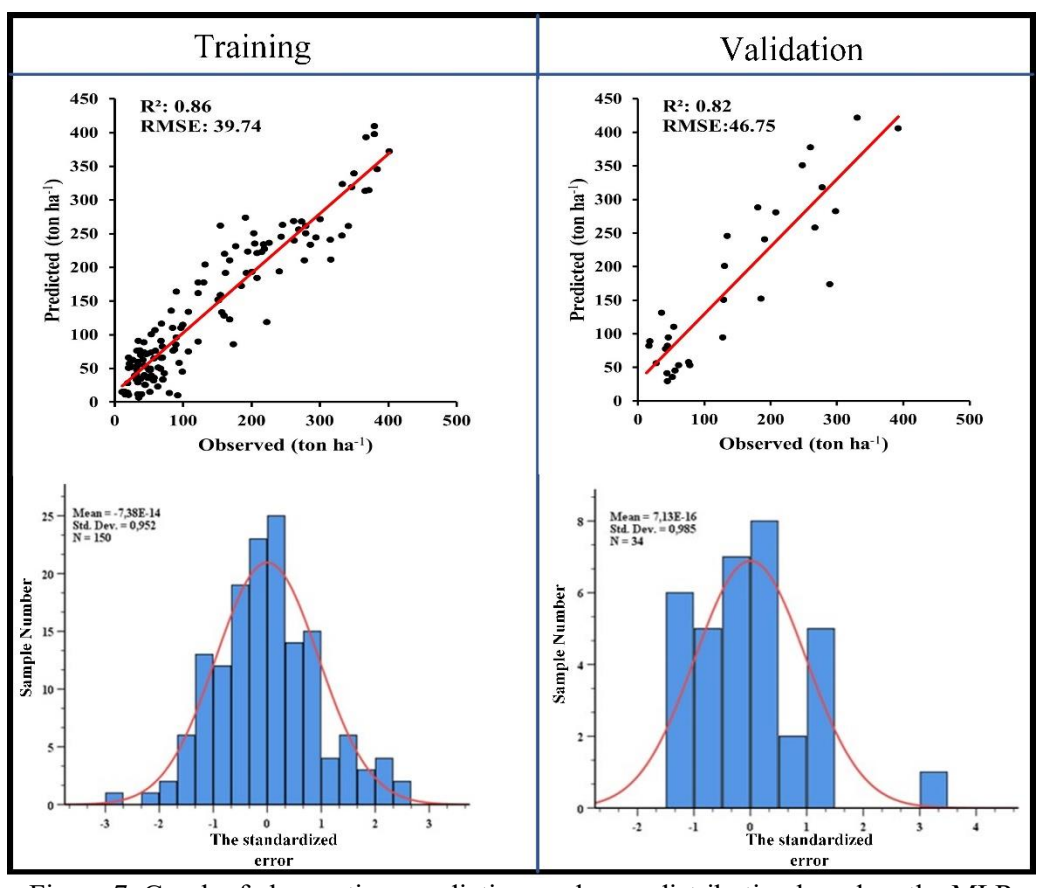


Figure 7. Graph of observation, prediction, and error distribution based on the MLR

Results of Multiple Linear Regression Analysis

AGC was modeled using the ANN technique, employing the independent variables from the model that achieved the highest predictive success with the MLR technique (Table 4). The results of the prediction models are presented in Table 5. In the ANN technique, 17 different models for AGC were developed by applying various learning rates and momentum values. The results of these ANN models are presented in Table 5. Upon reviewing Table 5, the most appropriate coefficient of determination and the lowest total relative rank were achieved in the AGC16 model (Model $R^2 = 0.89$, Test R^2 = 0.77, learning rate = 0.8, momentum = 0.1, $R_i = 13.44$). Although the model specification coefficients of AGC2, AGC6, AGC10, and AGC11 are identical to those of AGC16, the

overall relative ranks of these models are higher, making AGC16 the most successful model. The graph illustrating the model and test coefficients of determination for AGC is shown in Figure 8. Furthermore, the graph depicting the changes in the coefficient of determination and total relative rank for the 17 ANN models obtained for AGC is presented in Figure 9. The prediction and observation graphs of AGC, as predicted by the ANN method for the model-test data sets, are shown in Figure 10.

Table 5. Values for the success criteria and total relative ranks in the artificial neural networks (ANNs)

	Parameters					Training					Validation							
Model												Total						Total
No	Lr.	Mo.	Input	Output	Hl.	Neuron	\mathbb{R}^2	RMSE	MAE	BIC	AIC	Relative	\mathbb{R}^2	RMSE	MAE	BIC	AIC	Relative
												Rank						Rank
AGC1	0.1	0.1	14	1	1	2	0.83	45.24	34.29	6.45	31.81	73.77	0.74	56.78	46.61	6.68	32.04	64.62
AGC2	0.1	0.2	14	1	1	2	0.89	36.19	26.43	6.23	31.59	18.81	0.71	59.52	43.76	6.73	32.09	69.76
AGC3	0.1	0.3	14	1	1	2	0.86	40.67	31.81	6.34	31.71	42.98	0.69	61.79	50.25	6.76	32.12	79.72
AGC4	0.1	0.4	14	1	1	2	0.88	37.23	27.52	6.26	31.62	14.96	0.71	59.62	45.88	6.73	32.09	71.31
AGC5	0.1	0.5	14	1	1	2	0.88	37.35	28.02	6.26	31.62	16.67	0.68	63.21	47.79	6.79	32.15	81.66
AGC6	0.1	0.6	14	1	1	2	0.89	35.9	26.54	6.22	31.58	5.2	0.74	57.11	45.58	6.68	32.04	64.79
AGC7	0.1	0.7	14	1	1	2	0.89	37.1	26.72	6.25	31.61	12.68	0.77	53.94	40.88	6.63	31.99	53.62
AGC8	0.1	0.8	14	1	1	2	0.87	39.89	29.55	6.33	31.69	34.34	0.76	54.61	44.67	6.64	32	57.75
AGC9	0.1	0.9	14	1	1	2	0.82	46.99	35.07	6.49	31.85	85	0.68	63.42	52.12	6.79	32.15	85
AGC10	0.2	0.1	14	1	1	2	0.89	37.04	26.45	6.25	31.61	11.9	0.71	59.74	47.28	6.73	32.09	72.6
AGC11	0.3	0.1	14	1	1	2	0.89	36.82	28	6.25	31.61	13.31	0.7	61.23	47.97	6.75	32.11	76.78
AGC12	0.4	0.1	14	1	1	2	0.88	37.85	28.74	6.27	31.63	20.92	0.72	59	47.64	6.72	32.08	70.97
AGC13	0.5	0.1	14	1	1	2	0.88	37.31	26.99	6.26	31.62	14.33	0.77	53.56	41.38	6.62	31.98	52.92
AGC14	0.6	0.1	14	1	1	2	0.88	37.66	28.35	6.27	31.63	19.13	0.74	56.99	45.92	6.68	32.04	64.71
AGC15	0.7	0.1	14	1	1	2	0.88	36.8	29.68	6.24	31.61	17.14	0.87	38.99	27.59	6.3	31.66	55
AGC16	0.8	0.1	14	1	1	2	0.89	36.93	27.69	6.25	31.61	13.44	0.77	53.79	41.58	6.62	31.99	53.65
AGC17	0.9	0.1	14	1	1	2	0.88	37.64	28.05	6.27	31.63	18.47	0.73	57.72	44.98	6.69	32.06	65.89

Lr: Learning Rate, Mo: Momentum, Hl: Hidden Layer, AGC1: Aboveground biomass 1st model

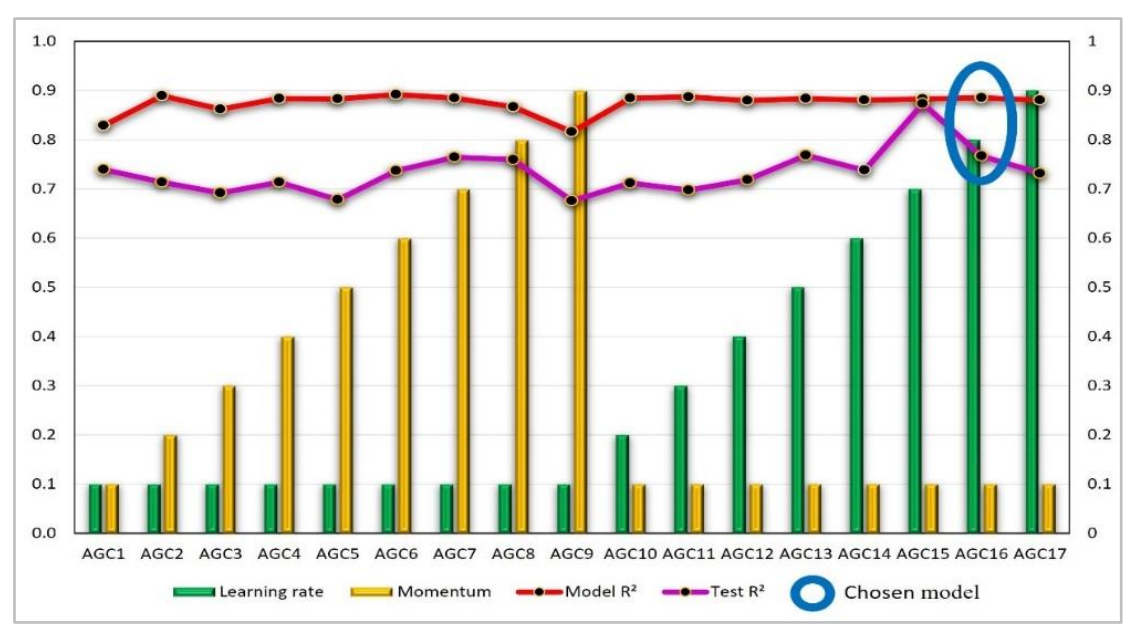


Figure 8. Graph of the coefficient of determination for aboveground carbon obtained using the ANNs model

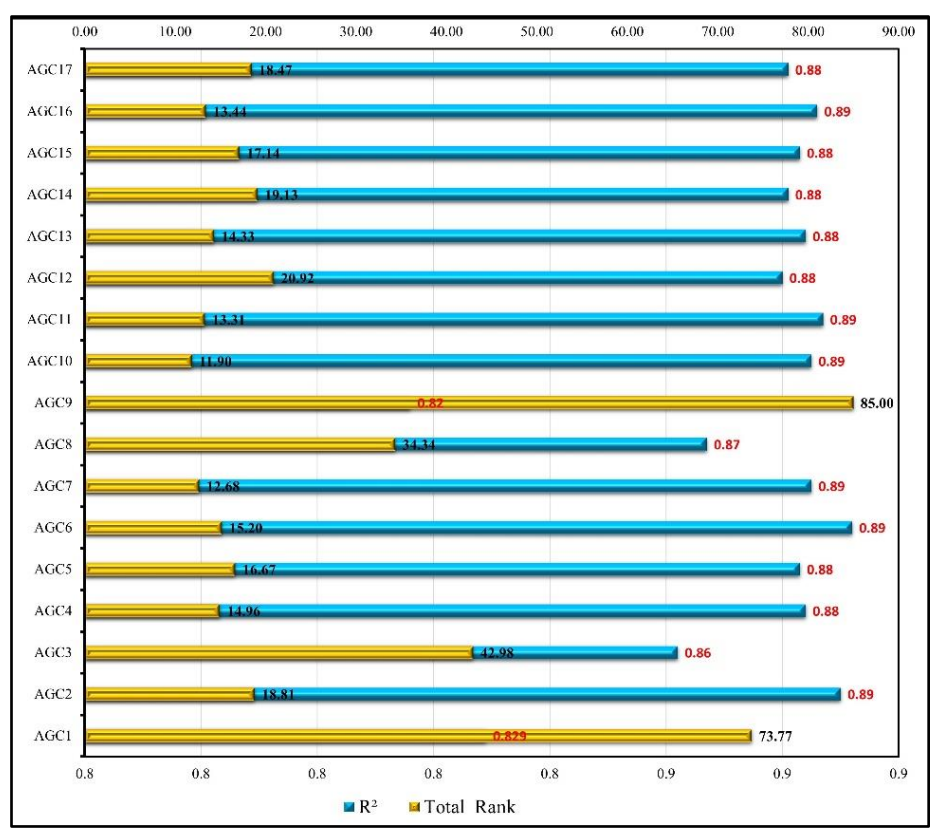


Figure 9. Variation in the models derived from remote sensing data based on the coefficient of determination and total relative rank values

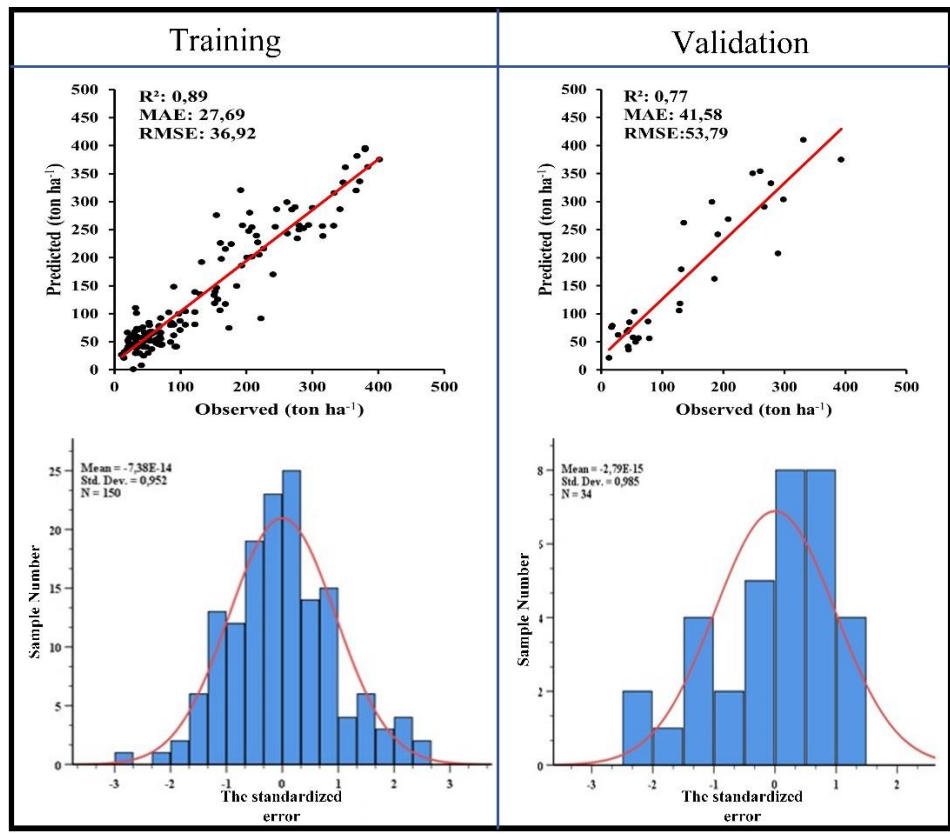


Figure 10. Graph of observation, prediction, and error distribution based on the ANNs model

Additionally, a paired t-test was conducted to assess the compatibility of the test predictions with the observed data. The test results indicated that the models were applicable to the stands in the study area at a significance

level of 0.05. The performance measures (R², MAE, AIC, BIC, BIAS, RMSE) and paired t-test results for the most successful AGC model predictions obtained through the modeling techniques are presented in Table 6.

Table 6. Performance metrics of the model obtained using the 15x15 texture data from the S2 for AGC

	Method	\mathbb{R}^2	RMSE	MAE	BIC	AIC	BIAS	Pa	aired
Training	MLR	0.86	39.74	31.17	5.88	21.68	-7.38×10 ⁻¹⁴	t-	test
	ANN	0.89	36.93	27.69	6.25	31.61	-7.38×10 ⁻¹⁴	t	p value
Validation	MLR	0.82	46.75	38.24	6.48	31.84	7.13×10 ⁻¹⁶	-2.054	0.726
	ANN	0.77	53.79	41.58	6.62	31.99	-2.79×10 ⁻¹⁵	-1.365	0.119

Discussion

In this study, AGC was modeled, and predictions were obtained using data sets from S1, S2, L8 and UAV. Two different techniques, MLR and ANN, were used in modeling. Upon examining the results of AGC modeling, the highest performance across all datasets used in the study was achieved with the texture values from the 15x15 window size derived from the S2 3). High model specification coefficients were obtained in both MLR and ANN methods (MLR R²=0.86, ANN R²=0.89). Similarly, the test coefficients of determination of both methods were also high (MLR R^2 =0.82, ANN R^2 =0.77). When the paired t-test results of the test data for AGC in MLR and ANN methods are analyzed, the pvalues are calculated as 0.726 and 0.119 for MLR and ANN, respectively (Table 6). Considering both the model and test specification coefficients and the p-value for the paired t-test for AGC, MLR was found to be the most applicable modeling technique. In both methods, the p-value for the paired t-test is greater than 0.05, indicating that the model network is feasible. Günlü and Ercanlı (2020), in their study to estimate AGC in pure beech stands using Alos Palsar L-band imagery, calculated the AGC of 153 sample plots by ground measurements, and for each sample plot, different window sizes $(3\times3, 5\times5, 7\times7,$ 9×9 and 11×11) and eight texture attributes (correlation, second moment, dissimilarity, entropy, contrast, variance, homogeneity and mean) with MLR and ANN modeling techniques. When the results obtained are analyzed, it is seen that the ability of ANN to

predict AGC is better than MLR (ANN $R^2 = 0.52$, MLR $R^2 = 0.38$). When compared to the AGC model results obtained using the S1 used in our study, it is seen that a very high success is achieved (Table 3).

Keleş et al., (2021) modeled AGC using SVM and MLR modeling techniques with backscatter values, band and vegetation index values at different polarizations from S1 and S2. They obtained the best result with the SVM modeling technique ($R^2 = 0.88$). In the MLR method, they calculated the R^2 as 0.75. When the results are compared with our study, it is seen that similar results are obtained. Poorazimy et al., (2020) estimated the AGC stock by using MLR and nonparametric k-NN, SVR and RF algorithms, using data from Airborne Lidar (ALS), Alos-2 L-band and UltraCam images alone and in combination. The results showed a low success rate of R^2 = 0.34 with ALS data and $R^2 = 0.41$ with the combination of data. They found similar results with the model performance values obtained from the UAV data sets of our study. Zhang et al., (2023) investigated the estimation and temporal variation of AGC using MLR and DL methods with Landsat satellite images. The results showed that the DL method ($R^2 = 0.64$) was more successful than the MLR method $(R^2 = 0.34)$. In comparison to our results, it is evident that the texture dataset derived from Landsat images is highly effective in modeling AGC and contributes significantly to achieving high levels of success. This study also involves modeling the relationships between AGC and variables such as digital band, reflectance, and vegetation index obtained from UAV imagery.

This study also encompasses the modeling of the relationships between AGC, and variables such as digital band, reflectance, and vegetation index obtained from UAV imagery. When the modeling results were evaluated, in contrast to the relationships obtained with satellite data sources, very low model successes were obtained in modeling AGC with UAV data. The coefficients of determination ranged between R²=0.24 for band reflectance and R²=0.34 for vegetation indices. Lower model successes were obtained compared to the model successes created with the datasets obtained from satellite imagery (Table 3). A significant model for AGC could not be developed using the digital band values from the UAV imagery dataset. The main reason for this can be explained by the number of pixels representing the sample areas. In satellite imagery, a sample area may be represented by just a few pixels, whereas in UAV imagery, the same area is represented by a greater number of pixels, resulting in changes to the homogeneity of the sample area data. When extracting reflectance values from 2.5 cm resolution UAV images for the sample areas, the average reflectance values capture not only reflections from treetops but also from gaps, substrates, and the forest floor. Including reflections from objects in the forest understory and floor layers introduces more variation in the average reflectance values within the sample area, thereby expanding the dataset's range. All this explains the discrepancy between the results of the UAV and satellite imagery and shows proportional relationship between resolution and the diversity of reflectance values.

This directly affects the performance of the model. To address this issue, it is anticipated that using tree-specific reflectance values derived from UAV imagery can help standardize reflectance values and enhance model performance by reducing the number of pixels representing the entire sample area. The following single-tree-based studies provide support for this conclusion. In their study aimed at estimating carbon stock using UAV, Abdullah et al. (2021) achieved a coefficient of determination of $R^2 = 0.66$.

In our study, the highest coefficient of determination was obtained with vegetation index values obtained from UAV images (R²=0.38). It can be said that the higher success of the aforementioned study can be attributed to the fact that, unlike our study, estimation was made using single tree-based data. Muhsoni et al., (2021) aimed to model the carbon of a mangrove tree using UAV images, and the results show that they obtained successful results in modeling with MLR technique ($R^2=0.75$). It is thought that the reason for their higher success compared to our study is again due to single tree-based modeling. Qin et al. (2021) evaluated the potential of combining UAV LIDAR data with hyperspectral imagery to estimate carbon in individual trees. Their results indicated that using LIDAR and hyperspectral data separately yielded carbon estimates with R² values of 0.74 and 0.75, respectively. They discovered that merging both LIDAR and hyperspectral data improved the accuracy of tree-level carbon stock estimation, with an R² value of 0.89. Upon reviewing the existing literature on UAVs, it becomes evident that there are limited studies focusing on AGC estimation using variables derived from UAV imagery, particularly in natural forests. The literature review on UAVs reveals that there are limited studies on AGC estimation using variables derived from UAV imagery, particularly in natural forests. As highlighted earlier, most studies primarily focus on estimating AGC for individual trees by integrating UAV imagery with satellite data such as S1, S2, L8, and LIDAR. Moreover, the literature on UAV data usage primarily concentrates on estimating AGC using singletree characteristics such as diameter and height derived from UAV imagery (RGB and NIR bands) or LIDAR data integrated with UAV imagery (Ye et al., 2019; Liu et al., 2022; Lin et al., 2022; Basyuni et al., 2023). Bulut et al. (2024) attempted to model tree height and tree volume using drone imagery datasets. They found coefficients of determination of 0.96 for tree height and 0.72 for tree volume. These high coefficients of determination in their study can be attributed to the creation of datasets based on individual tree reflectance values, in contrast to our approach. As mentioned above, the successful model

predictions with UAV imagery show that modeling with datasets obtained from individual tree data will yield higher results. In this study, the datasets for UAV imagery were calculated over sample plots rather than individual trees. Therefore, high resolution UAV images (2.5 cm - 3.5 cm) provide a lot of detail and different reflectance values are obtained from these details. This causes a lot of variability in the sample plot image values. Therefore, this situation negatively affects modeling success. The reason why the datasets in this study are created on a sample plot basis is that it should be the same as the logic of creating a satellite image dataset. Because the study investigated whether UAV images can be an alternative data source to satellite images in modeling. The results show that UAV datasets created in a similar process to satellite image processing and dataset creation processes show lower model success and therefore cannot be an alternative to satellite imagery in this approach.

Conclusions

In this study, MLR and ANN modeling techniques were used to estimate AGC in pure yellow pine stands in northern Turkey using data from L8, S2, S1 and UAV images. The results showed that the texture values obtained from the S2 were able to predict AGC better with the MLR method compared to other images and variables and ANN analysis. The analysis of performance criteria across all datasets related to MLR revealed that the most successful model was achieved by using the texture values from the S2 15x15 window size as the independent variables. The lowest model successes were found in the models developed with the backscatter and band brightness values generated from the S1. When the digital band values obtained from UAV images were analyzed in relation to AGC, no significant model was found, indicating the limited success of using UAVs in predicting AGC. Model successes for modeling AGC with vegetation indices values were 0.34, 0.43, and 0.64 for UAV, L8 and S2, respectively. As a result, the texture variables obtained from S2 images with MLR showed superior performance in AGC estimation compared to other satellite images and variables derived from them. The results

obtained from this study can potentially provide valuable information for application in comparable forest ecosystems. In future research, combining variables from both active and passive satellite imagery, topographic integrating data, investigating various modeling techniques such as XGBoost, RF, SVM, ensemble methods, and MARS could significantly improve the model's success in predicting AGC.

Acknowledgements

This study was produced from a doctoral thesis prepared by Hasan AKSOY and supervised by Prof. Dr. Alkan GÜNLÜ for the Institute of Natural and Applied Science, Çankırı Karatekin University, Türkiye.

Ethics Committee Approval

N/A

Peer-review

Externally peer-reviewed.

Author Contributions

Conceptualization: H.A., A.G.; Investigation: H.A.; Material and Methodology: H.A., A.G.; Visualization: H.A., A.G.; Writing-Original Draft: H.A., A.G.; Writing-review & Editing: H.A., A.G. All authors have read and agreed to the published version of the manuscript.

Conflict of Interest

The authors declare that they have no conflict of interest.

Funding

This study was funded by the Scientific Research Project Unit of Cankırı Karatekin University (Grant No: OF211221D08).

References

Abdullah, M. M., Al-Ali, Z. M. & Srinivasan, S. (2021). The use of UAV-based remote sensing to estimate biomass and carbon stock for native desert shrubs. *MethodsX*, 8, 101399. https://doi.org/10.1016/j.mex.2021.101399

Aertsen, W., Kint, V., van Orshoven, J., Özkan, K. & Muys, B. (2010). Comparison and ranking of different modelling techniques for prediction of site index in Mediterranean mountain forests. *Ecological Modelling*,

- 221(8),1119-1130. https://doi.org/10.1016/j.ecolmodel.2010.01.0 07
- Akıllı, A. & Hülya, A. (2020). Evaluation of normalization techniques on neural networks for the prediction of 305-day milk yield. *Turkish Journal of Agricultural Engineering Research*, 1(2), 354-367. https://doi.org/10.46592/turkager.2020.v01i02.011
- Aksoy, H. (2022). Sinop Orman Bölge Müdürlüğü Saf Sarıçam Meşcerelerinde Farklı Uzaktan Algılama Verileri Kullanılarak Bazı Meşcere Parametrelerinin Modellenmesi (Doctoral dissertation, Doktora Tezi, Çankırı Karatekin Üniversitesi, Çankırı).
- Aksoy, H. (2024). Estimation Stand Volume, Basal Area and Quadratic Mean Diameter Using Landsat 8 OLI and Sentinel-2 Satellite Image With Different Machine Learning Techniques. *Transactions* in GIS. https://doi.org/10.1111/tgis.13265
- Aksoy, H., & Günlü, A. (2025). UAV and satellite-based prediction of aboveground biomass in scots pine stands: a comparative analysis of regression and neural network approaches. *Earth Science Informatics*, 18(1), 66. https://doi.org/10.1007/s12145-024-01657-0
- Aksoy, H. (2024). Evaluation of forest areas and land use/cover (LULC) changes with a combination of remote sensing, intensity analysis and CA-Markov modelling. *New Zealand Journal of Forestry Science*, 54. https://doi.org/10.33494/nzjfs542024x328x
- Alquraish, M. M. & Khadr, M. (2021). Remote-sensing-based streamflow forecasting using artificial neural network and support vector machine models. *Remote Sensing*, 13(20), 4147. https://doi.org/10.3390/rs13204147
- Baloloy, A. B., Blanco, A. C., Candido, C.G., Argamosa, R. J. L., Dumalag, J. B. L. C., et al. (2018). Estimation of mangrove forest aboveground biomass using multispectral bands, vegetation indices and biophysical variables derived from optical satellite imageries: Rapideye, planetscope and sentinel-2. *ISPRS Annals of the Photogrammetry, Remote Sensing and Spatial Information Sciences*, 4, 29-36. https://doi.org/10.5194/isprs-annals-IV-3-29-2018
- Basyuni, M., Wirasatriya, A., Iryanthony, S.B., Amelia, R., Slamet, B., et al. (2023). Aboveground biomass and carbon stock estimation using UAV photogrammetry in Indonesian mangroves and other competing land uses. *Ecological Informatics*, 77, 102227. https://doi.org/10.
 - 1016/j.ecoinf.2023.102227

- Bendig, J., Yu, K., Aasen, H., Bolten, A., Bennertz, S., Broscheit, J., ... & Bareth, G. (2015). Combining UAV-based plant height from crop surface models, visible, and near infrared vegetation indices for biomass monitoring in barley. International Journal of Applied Earth Observation and Geoinformation, 39, 79-87. https://doi.org/10.1016/j.jag.2015.02.012
- Bi, H., Murphy, S., Volkova, L., Weston, C., Fairman, T., et al. (2015). Additive biomass equations based on complete weighing of sample trees for open eucalypt forest species in south-eastern Australia. *Forest Ecology and Management*, 349, 106-121. https://doi.org/10.1016/j.foreco.2015.03.007
- Blackburn, G. A. (1998). Spectral indices for estimating photosynthetic pigment concentrations: a test using senescent tree leaves. International Journal of remote sensing, 19(4), 657-675. https://doi.org/10.1080/014311698215919
- Bolat, F. (2021). Ankara Orman Bölge Müdürlüğü Anadolu Karaçamı meşcerelerinde artım ve büyümenin yapay sinir ağları ile modellenmesi. Doktora Tezi, Çankırı Karatekin Üniversitesi, Çankırı.
- Bulut, S. (2023). Machine learning prediction of above-ground biomass in pure Calabrian pine (Pinus brutia Ten.) stands of the Mediterranean region, Türkiye. *Ecological Informatics*, 74, 101951. https://doi.org/10.1016/j.ecoinf.2022.101951
- Bulut, S., Günlü, A., Aksoy, H., Bolat, F. & Sönmez, M. Y. (2024). Integration of field measurements with unmanned aerial vehicle to predict forest inventory metrics at tree and stand scales in natural pure Crimean pine forests. *International Journal of Remote Sensing*, 45(12), 3872-3896. https://doi.org/10.1080/01431161.2024.23578
- Chen, J. M. (1996). Evaluation of vegetation indices and a modified simple ratio for boreal applications. Canadian Journal of Remote Sensing, 22(3), 229-242. https://doi.org/10.1080/07038992.1996.10855
- Cheng, W. X., Yang, C. J., Zhou, W. C. & Liu, Y. C. (2009). Research summary of forest volume quantitative estimation based on remote sensing technology. *J. Anhui Sci*, 37, 7746-7750.
- Chrysafis, I., Mallinis, G., Tsakiri, M. & Patias, P. (2019). Evaluation of single-date and multiseasonal spatial and spectral information of Sentinel-2 imagery to assess growing stock volume of a Mediterranean forest. International *Journal of Applied Earth Observation and*

- *Geoinformation*, 77, 1-14. https://doi.org/10.1016/j.jag.2018.12.004
- Dong, L., Tang, S., Min, M., Veroustraete, F. & Cheng, J. (2019). Aboveground forest biomass based on OLSR and an ANN model integrating LiDAR and optical data in a mountainous region of China. International *Journal of Remote Sensing*, 40(15), 6059-6083. https://doi.org/10.1080/01431161.2019.15872
- Du, M., & Noguchi, N. (2017). Monitoring of wheat growth status and mapping of wheat yield's within-field spatial variations using color images acquired from UAV-camera system. Remote sensing, 9(3), 289. https://doi.org/10.3390/rs9030289
- Ehlers, D., Wang, C., Coulston, J., Zhang, Y., Pavelsky, T., et al. (2022). Mapping forest aboveground biomass using multisource remotely sensed data. *Remote Sensing*, 14(5), 1115. https://doi.org/10.3390/rs14051115
- Ercanlı, İ., Kurt, A., Şenyurt, M., Günlü, A., Bolat, F, et al. (2018). Tarsus Yöresi Anadolu Karaçamı Ağaçlarında Hacim Tahminlerinin Yapay Sinir Ağları ile Elde Edilmesi. *Anadolu Orman Araştırmaları Dergis*i, 4(1), 25-37.
- Fernandes, M.R., Aguiar, F.C., Martins, M.J., Rico, N., Ferreira, M.T, et al. (2020). Carbon stock estimations in a mediterranean riparian forest: A case study combining field data and UAV imagery. *Forests*, 11(4), 376. https://doi.org/10.3390/f11040376
- Foresee, F. D. & Hagan, M. T. (1997). Gauss-Newton approximation to Bayesian learning. In Proceedings of international conference on neural networks (ICNN'97) (Vol. 3, pp. 1930-1935). *IEEE*. https://doi.org/10.1109/ICNN.1997.614194
- Fremout, T., Cobián-De Vinatea, J., Thomas, E., Huaman-Zambrano, W., Salazar-Villegas, M., et al. (2022). Site-specific scaling of remote sensing-based estimates of woody cover and aboveground biomass for mapping long-term tropical dry forest degradation status. *Remote Sensing of Environment*, 276, 113040. https://doi.org/10.1016/j.rse.2022.113040
- Fu, Y. (2018). Aboveground biomass estimation and uncertainties assessing on regional scale with an improved model analysis method. *Hubei For. Sci. Technol*, 47, 1-4.
- Gamon JA, Surfus JS (1999) Assessing leaf pigment content and activity with a reflectometer. New Phytol 143(1):105–117
- García-Fernández, M., Sanz-Ablanedo, E., & Rodríguez-Pérez, J. R. (2021). High-resolution drone-acquired RGB imagery to estimate

- spatial grape quality variability. Agronomy, 11(4),655.https://doi.org/10.3390/agronomy11 040655
- GDF, (2022). Sinop Regional Directorate of Forestry, Forest Planing Units, Forest Management Plans. Republic of Turkey, General Directorate of Forestry, Forest Administration and Planning Department, Ankara.
- Georgopoulos, N., Sotiropoulos, C., Stefanidou, A. & Gitas, I. Z. (2022). Total Stem Biomass Estimation Using Sentinel-1 and-2 Data in a Dense Coniferous Forest of Complex Structure and Terrain. *Forests*, 13(12), 2157. https://doi.org/10.3390/f13122157
- Gitelson AA, Kaufman YJ, Stark R, Rundquist D (2002) Novel algorithms for remote estimation of vegetation fraction. Remote Sens Environ 80(1):76–87. https://doi.org/10.1016/S0034-4257(01)00289-9
- Gitelson, A. A., Kaufman, Y. J., & Merzlyak, M. N. (1996). Use of a green channel in remote sensing of global vegetation from EOS-MODIS. Remote sensing of Environment, 58(3), 289-298. https://doi.org/10.1016/S0034-4257(96)00072-7
- Goel, N. S., & Qin, W. (1994). Influences of canopy architecture on relationships between various vegetation indices and LAI and FPAR: A computer simulation. Remote Sensing Reviews, 10(4), 309347.
 - https://doi.org/10.1080/02757259409532252
- Guisan, A., Edwards Jr, T. C. & Hastie, T. (2002). Generalized linear and generalized additive models in studies of species distributions: setting the scene. *Ecological Modelling*, 157(2-3), 89-100. https://doi.org/10.1016/S0304-3800(02)00204-1
- Günlü, A. & Ercanlı, İ. (2020). Artificial neural network models by ALOS PALSAR data for aboveground stand carbon predictions of pure beech stands: a case study from northern of Turkey. *Geocarto International*, 35(1), 17-28. https://doi.org/10.1080/10106049.2018.14998
- Günlü, A., Ercanli, I., Başkent, E. Z. & Çakır, G. (2014). Estimating aboveground biomass using Landsat TM imagery: A case study of Anatolian Crimean pine forests in Turkey. *Annals of Forest Research*, 57(2), 289-298. https://doi.org/10.15287/afr.2014.278
- Günlü, A., Ercanlı, İ., Şenyurt, M. & Keleş, S. (2021). Estimation of some stand parameters from textural features from WorldView-2 satellite image using the artificial neural network and multiple regression methods: a case study from Türkiye. *Geocarto*

- *International*, 36(8), 918-935. https://doi.org/10.1080/10106049.2019.1629644
- Hague, T., Tillett, N. D., & Wheeler, H. (2006). Automated crop and weed monitoring in widely spaced cereals. Precision Agriculture, 7, 21-32. https://doi.org/10.1007/s11119-005-6787-1
- Hamidi, S. K., Weiskittel, A., Bayat, M. & Fallah, A. (2021). Development of individual tree growth and yield model across multiple contrasting species using nonparametric and parametric methods in the Hyrcanian forests of northern Iran. *European Journal of Forest Research*, 140(2), 421-434. https://doi.org/10.1007/s10342-020-01340-1
- Han, H., Wan, R. & Li, B. (2021). Estimating forest aboveground biomass using Gaofen-1 images, Sentinel-1 images, and machine learning algorithms: A case study of the Dabie Mountain Region, China. *Remote Sensing*, 14(1), 176. https://doi.org/10.3390/rs14010176
- Huang, H., Liu, C., Wang, X., Zhou, X. & Gong, P. (2019). Integration of multi-resource remotely sensed data and allometric models for forest aboveground biomass estimation in China. Remote Sensing of Environment, 221, 225-234. https://doi.org/10.1016/j.rse.2018.11. 017
- Huete AR (1988) A soil-adjusted vegetation index (SAVI). Remote Sens Environ 25(3):295–309. https://doi.org/10.1016/0034-4257(88)90106-X
- Hunt ER Jr, Doraiswamy PC, McMurtrey JE, Daughtry CS, Perry EM, Akhmedov B (2013) A visible band index for remote sensing leaf chlorophyll content at the canopy scale. Int J Appl Earth Obs Geoinf 21:103–112. https://doi.org/10.1016/j.jag.2012.07.020
- Hunt ER Jr, Rock BN (1989) Detection of changes in leaf water content using near-and middle-infrared reflectances. Remote Sens Environ 30(1):43–54. https://doi.org/10.1016/0034-4257(89)90046-1
- Jiang, Z., Huete, A. R., Didan, K., & Miura, T. (2008). Development of a two-band enhanced vegetation index without a blue band. Remote sensing of Environment, 112(10), 3833-3845. https://doi.org/10.1016/j.rse.2008.06.006
- Jucker, T., Caspersen, J., Chave, J., Antin, C., Barbier, N., et al. (2017). Allometric equations for integrating remote sensing imagery into forest monitoring programmes. *Global Change Biology*, 23(1), 177-190. https://doi.org/10.1111/gcb.13388
- Keleş, S., Günlü, A. & Ercanli, İ. (2021). Estimating aboveground stand carbon by combining Sentinel-1 and Sentinel-2 satellite data: a case study from Turkey. In Forest

- Resources Resilience and Conflicts (pp. 117-126). Elsevier. https://doi.org/10.1016/B978-0-12-822931-6.00008-3
- Key CH, Benson NC (2006) Landscape assessment (LA). FIREMON: Fire effects monitoring and inventory system, 164, LA-1
- Lan, Y. B., Zhu, Z. H., Deng, X. L., Lian, B. Z., Huang, J. Y., et al (2019). Monitoring and classification of citrus Huanglongbing based on UAV hyperspectral remote sensing. *Transactions of the CSAE*, 35(3), 92-100.
- Lawrence, S., Giles, C. L. & Tsoi, A. C. (1997). Lessons in neural network training: Overfitting may be harder than expected. In *Aaai/iaai* (pp. 540-545).
- Li, C., Li, M., Li, Y. & Qian, P. (2020a). Estimating aboveground forest carbon density using Landsat 8 and field-based data: A comparison of modelling approaches. *International Journal of Remote Sensing*, 41(11), 4269-4292. https://doi.org/10.1080/01431161.2020.17147
- Li, Y., Li, M., Li, C. & Liu, Z. (2020b). Forest aboveground biomass estimation using Landsat 8 and Sentinel-1A data with machine learning algorithms. *Scientific reports*, 10(1), 9952. https://doi.org/10.1038/s41598-020-67024-3
- Lin, J., Chen, D., Wu, W. & Liao, X. (2022). Estimating aboveground biomass of urban forest trees with dual-source UAV acquired point clouds. *Urban Forestry & Urban Greening*, 69, 127521. https://doi.org/10.1016/j.ufug.2022.127521
- Listopad, C. M., Drake, J. B., Masters, R. E. & Weishampel, J. F. (2011). Portable and airborne small footprint LiDAR: Forest canopy structure estimation of fire managed plots. *Remote Sensing*, 3(7), 1284-1307. https://doi.org/10.3390/rs3071284
- Liu HQ, Huete A (1995) A feedback based modification of the NDVI to minimize canopy background and atmospheric noise. IEEE Trans Geosci Remote Sens 33(2):457–465
- Liu, N., Sun, P., Caldwell, P. V., Harper, R., Liu, S., et al. (2020). Trade-off between watershed water yield and ecosystem productivity along elevation gradients on a complex terrain in southwestern China. *Journal of Hydrology*, 590, 125449. https://doi.org/10.1016/j.jhydrol.2020.125449
- Liu, Y., Feng, H., Yue, J., Fan, Y., Jin, X., et al. (2022). Estimation of Potato Above-Ground Biomass Based on Vegetation Indices and Green-Edge Parameters Obtained from UAVs. *Remote Sensing*, 14(21), 5323. https://doi.org/10.3390/rs14215323

- Louhaichi M, Borman MM, Johnson DE (2001) Spatially located platform and aerial photography for documentation of grazing impacts on wheat. Geocarto Int 16(1):65–70. https://doi.org/10.1080/10106040108542184
- Lu, D., Chen, Q., Wang, G., Moran, E., Batistella, M., et al. (2012). Aboveground forest biomass estimation with Landsat and LiDAR data and uncertainty analysis of the estimates. *International Journal of Forestry Research*, 2012. https://doi.org/10.1155/2012/436537
- McFeeters, S. K. (1996). The use of the Normalized Difference Water Index (NDWI) in the delineation of open water features. International journal of remote sensing, 17(7), 1425-1432.
 - https://doi.org/10.1080/01431169608948714
- Mu, B., Zhao, X., Zhao, J., Liu, N., Si, L., et al. (2022). Quantitatively Assessing the Impact of Driving Factors on Vegetation Cover Change in China's 32 Major Cities. *Remote Sensing*, 14(4), 839. https://doi.org/10.3390/rs14040839
- Muhsoni, F. F., Abida, I. W., Rini, D. A. S. & Putera, A. J. (2021). Estimation of mangrove carbon using drone images. *Depik*, 10(1), 41-46. https://doi.org/10.13170/depik.10.1.19313
- Ogana, F. N. & Ercanli, I. (2022). Modelling height-diameter relationships in complex tropical rain forest ecosystems using deep learning algorithm. *Journal of Forestry Research*, 33(3), 883-898. https://doi.org/10.1007/s11676-021-01373-1
- Okut, H. (2016). Bayesian regularized neural networks for small n big p data. *Artificial Neural Networks-Models and applications*, 28. https://dx. doi.org/10.5772/63256
- Ou, G., Li, C., Lv, Y., Wei, A., Xiong, H., et al. (2019). Improving aboveground biomass estimation of Pinus densata forests in Yunnan using Landsat 8 imagery by incorporating age dummy variable and method comparison. *Remote Sensing*, 11(7), 738. https://doi.org/10.3390/rs11070738
- Poorazimy, M., Shataee, S., McRoberts, R. E. & Mohammadi, J. (2020). Integrating airborne laser scanning data, space-borne radar data and digital aerial imagery to estimate aboveground carbon stock in Hyrcanian forests, Iran. *Remote Sensing of Environment*, 240, 111669. https://doi.org/10.1016/j.rse.2020.111669
- Poudel, K. P. & Cao, Q. V. (2013). Evaluation of methods to predict Weibull parameters for characterizing diameter distributions. *Forest Science*, 59(2), 243-252. https://doi.org/10.5849/forsci.12-001
- Qin, H., Zhou, W., Yao, Y. & Wang, W. (2021). Estimating aboveground carbon stock at the scale of individual trees in subtropical forests

- using UAV LiDAR and hyperspectral data. *Remote Sensing*, 13(24), 4969. https://doi.org/10.3390/rs13244969
- Romanov, A. A., Tamarovskaya, A. N., Gloor, E., Brienen, R., Gusev, B. A., et al. (2022). Reassessment of carbon emissions from fires and a new estimate of net carbon uptake in Russian forests in 2001–2021. *Science of The Total Environment*, 846, 157322. https://doi.org/10.1016/ j.scitotenv.2022.157322
- Rouse JW, Haas RH, Schell JA, Deering DW (1974) Monitoring vegetation systems in the Great Plains with ERTS. NASA Spec Publ 351(1):309
- Sakici, O. E., & Günlü, A. (2018). Artificial intelligence applications for predicting some stand attributes using Landsat 8 OLI satellite data: A case study from Turkey. https://aperta.ulakbim.gov.tr/record/34107/files/10-15666-aeer-1604
- Sakici, O. E., & Ozdemir, G. (2018). Stem taper estimations with artificial neural networks for mixed Oriental beech and Kazdaği fir stands in Karabük region, Turkey. Cerne, 24(4), 439-451.
- Seki, M. & Atar, D. (2021). Temporal and spatial change of carbon storage in Alara Forest Planning Unit. *Kastamonu University Journal of Forestry Faculty*, 21(3), 208-217. https://doi.org/10.17475/kastorman.1048387
- Seki, M. (2023). Predicting stem taper using artificial neural network and regression models for Scots pine (Pinus sylvestris L.) in northwestern Türkiye. Scandinavian Journal of Forest Research, 38(1-2), 97-104. https://doi.org/10.1080/02827581.2023.21892
- Silva, C. A., Saatchi, S., Garcia, M., Labriere, N., Klauberg, C., et al. (2018). Comparison of small-and large-footprint lidar characterization of tropical forest aboveground structure and biomass: a case study from Central Gabon. *IEEE Journal of Selected Topics in Applied Earth Observations and Remote Sensing*, 11(10), 3512-3526. https://doi.org/10.1109/JSTARS
- .2018.2816962
 Sivasankar, T., Lone, J. M., Sarma, K. K., Qadir^o, A. & Raju, P. L. N. (2013). Estimation of above ground biomass using support vector. *Vietnam Journal of Earth Sciences*, 41(2), 95-104.
- Skudnik, M. & Jevšenak, J. (2022). Artificial neural networks as an alternative method to nonlinear mixed-effects models for tree height predictions. *Forest Ecology and Management*, 507, 120017. https://doi.org/10.1016/j.foreco.2022.120017

- Strobl, R. O. & Forte, F. (2007). Artificial neural network exploration of the influential factors in drainage network derivation. *Hydrological Processes: An International Journal*, 21(22), 2965-2978. https://doi.org/10.1002/hyp.6506
- Tang, J., Liu, Y., Li, L., Liu, Y., Wu, Y., et al. (2022). Enhancing Aboveground Biomass Estimation for Three Pinus Forests in Yunnan, SW China, Using Landsat 8. *Remote Sensing*, 14(18), 4589. https://doi.org/10.3390/rs14184589
- Themistocleous K (2019), June DEM modeling using RGB-based vegetation indices from UAV images. In Seventh International Conference on Remote Sensing and Geoinformation of the Environment (RSCy2019) (Vol. 11174, pp. 499–506). SPIE. https://doi.org/10.1117/12.2532748
- Tucker, C. J. (1979). Red and photographic infrared linear combinations for monitoring vegetation. Remote sensing of Environment, 8(2), 127-150. https://doi.org/10.1016/0034-4257(79)90013-0
- Turgut, R. & Günlü, A. (2022). Estimating aboveground biomass using Landsat 8 OLI satellite image in pure Crimean pine (Pinus nigra JF Arnold subsp. pallasiana (Lamb.) Holmboe) stands: a case from Turkey. *Geocarto International*, 37(3), 720-734. https://doi.org/10.1080/10106049.2020.17379 71
- Udali, A., Lingua, E. & Persson, H.J. (2021). Assessing forest type and tree species classification using Sentinel-1 C-band SAR data in Southern Sweden. *Remote Sensing*, 13(16), 3237. https://doi.org/10.3390/rs13163237
- Van Havre, Z., White, N., Rousseau, J. & Mengersen, K. (2015). Overfitting Bayesian mixture models with an unknown number of components. *PloS one*, 10(7), e0131739. https://doi.org/10.1371/journal.pone.0131739
- Wang, S., Wang, D. & Sun, J. R. (2022). Artificial neural network-based ionospheric delay correction method for satellite-based augmentation systems. *Remote Sensing*, 14:676
- Wang, X., Shao, G., Chen, H., Lewis, B. J., Qi, G., et al. (2013). An application of remote sensing data in mapping landscape-level forest biomass for monitoring the effectiveness of forest policies in northeastern China. *Environmental Management*, 52, 612-620. https://doi.org/10.1007/s00267-013-00
- Woebbecke, D. M., Meyer, G. E., Von Bargen, K., & Mortensen, D. A. (1995). Shape features for

- identifying young weeds using image analysis. Transactions of the ASAE, 38(1), 271-281.
- Wu, M., Dong, G., Wang, Y., Xiong, R., Li, Y., et al. (2020). Estimation of forest aboveground carbon storage in Sichuan Miyaluo Nature Reserve based on remote sensing. *Acta Ecol. Sin*, 40(2), 621-628.
- Xu, C., Wang, B. & Chen, J. (2022). Forest carbon sink in China: Linked drivers and long short-term memory network-based prediction. Journal of Cleaner Production, 359, 132085. https://doi.org/10.1016/j.jclepro.2022.132085
- Yavaşlı, D.D., & Ölgen, M.K. (2017). modeling above ground biomass in calabrian pine forests of düzlerçami (ANTALYA). *Ege Coğrafya Dergisi*, 26(2), 151-161.
- Yavuz, H., Mısır, N., Tüfekçioğlu, A., Altun, L., Mısır, M., et al. (2010). Karadeniz Bölgesi saf ve karışık Sarıçam (Pinus slyvestris L.) meşcereleri için mekanistik büyüme modellerinin geliştirilmesi, biyokütle ve karbon depolama miktarlarının belirlenmesi. (TÜBİTAK-TOVAG Projesi, Proje No: 106O274), Karadeniz Teknik Üniversitesi Orman Fakültesi, Trabzon.
- Ye, N., van Leeuwen, L. & Nyktas, P. (2019). Analysing the potential of UAV point cloud as input in quantitative structure modelling for assessment of woody biomass of single trees. *International Journal of Applied Earth Observation and Geoinformation*, 81, 47-57. https://doi.org/10.1016/j.jag.2019.05.010
- Zaninovich, S. C. & Gatti, M. G. (2020). Carbon stock densities of semi-deciduous Atlantic forest and pine plantations in Argentina. *Science of the Total Environment*, 747, 141085. https://doi.org/10.1016/j.scitotenv.2020.141085
- Zarco-Tejada, P. J., Berjón, A., López-Lozano, R., Miller, J. R., Martín, P., Cachorro, V., ... & De Frutos, A. (2005). Assessing vineyard condition with hyperspectral indices: Leaf and canopy reflectance simulation in a rowstructured discontinuous canopy. Remote Sensing of Environment, 99(3), 271-287. https://doi.org/10.1016/j.rse.2005.09.002
- Zhang, F., Tian, X., Zhang, H. & Jiang, M. (2022). Estimation of aboveground carbon density of forests using deep learning and multisource remote sensing. *Remote Sensing*, 14(13), 3022. https://doi.org/10.3390/rs14133022
- Zhang, W., Zhao, L., Li, Y., Shi, J., Yan, M., et al. (2022). Forest Above-Ground Biomass Inversion Using Optical and SAR Images Based on a Multi-Step Feature Optimized Inversion Model. *Remote Sensing*, 14(7), 1608. https://doi.org/10.3390/rs14071608

- Zhang, X., Jia, W., Sun, Y., Wang, F. & Miu, Y. (2023). Simulation of Spatial and Temporal Distribution of Forest Carbon Stocks in Long Time Series—Based on Remote Sensing and Deep Learning. *Forests*, 14(3), 483. https://doi.org/10.3390/f14030483
- Zheng, D., Rademacher, J., Chen, J., Crow, T., Bresee, M., et al. (2004). Estimating aboveground biomass using Landsat 7 ETM+ data across a managed landscape in northern Wisconsin, USA. *Remote Sensing of Environment*, 93(3), 402-411. https://doi.org/10.1016/j.rse.2004.08.008